

## MIT Open Access Articles

*Orientation and size-dependent mechanical modulation within individual secondary osteons in cortical bone tissue*

The MIT Faculty has made this article openly available. **Please share** how this access benefits you. Your story matters.

**Citation:** Carnelli, Davide, Pasquale Vena, Ming Dao, Christine Ortiz, and Roberto Contro. "Orientation and Size-Dependent Mechanical Modulation Within Individual Secondary Osteons in Cortical Bone Tissue." *Journal of The Royal Society Interface* 10, no. 81 (January 24, 2013): 20120953–20120953.

**As Published:** <http://dx.doi.org/10.1098/rsif.2012.0953>

**Publisher:** Royal Society

**Persistent URL:** <http://hdl.handle.net/1721.1/92976>

**Version:** Author's final manuscript: final author's manuscript post peer review, without publisher's formatting or copy editing

**Terms of use:** Creative Commons Attribution-Noncommercial-Share Alike



**Orientation and Size Dependent Mechanical Modulation  
within Individual Secondary Osteons in Cortical Bone Tissue**

Journal:	<i>Journal of the Royal Society Interface</i>
Manuscript ID:	rsif-2012-0953.R1
Article Type:	Research
Date Submitted by the Author:	n/a
Complete List of Authors:	Carnelli, Davide; Politecnico di Milano, ; Massachusetts Institute of Technology, Vena, Pasquale; Politecnico di Milano, ; IRCCS, Istituto Ortopedico Galeazzi, Dao, Ming; Massachusetts Institute of Technology, Ortiz, Christine; Massachusetts Institute of Technology, Contro, Roberto; Politecnico di Milano,
Subject:	Biomechanics < CROSS-DISCIPLINARY SCIENCES
Keywords:	hierarchical structure, anisotropy, length scale effect, nanoindentation, secondary osteons

SCHOLARONE™  
Manuscripts

**Orientation and Size Dependent Mechanical Modulation within Individual Secondary Osteons in Cortical Bone Tissue**

Davide Carnelli<sup>1,3,δ</sup>, Pasquale Vena<sup>2,4</sup>, Ming Dao<sup>3</sup>, Christine Ortiz<sup>3</sup>, and Roberto Contro<sup>1</sup>

<sup>1</sup> LaBS-Laboratory of Biological Structure Mechanics, Department of Structural Engineering, Politecnico di Milano, P.zza L. da Vinci 32, 20133, Milan, Italy.

<sup>2</sup> LaBS-Laboratory of Biological Structure Mechanics, Chemistry, Material and Chemical Engineering Department, Politecnico di Milano, P.zza L. da Vinci 32, 20133, Milan, Italy.

<sup>3</sup> Department of Materials Science and Engineering, Massachusetts Institute of Technology, 77 Massachusetts Avenue, 02139, Cambridge, MA, USA.

<sup>4</sup> IRCCS, Istituto Ortopedico Galeazzi, P.zza R. Galeazzi 4, 20161, Milano, Italy

<sup>δ</sup> Current Address: Complex Materials, Department of Materials, ETH Zürich, Wolfgang-Pauli-Str. 10, 8093 Zürich, Switzerland

**Address for correspondence:**

Dr. Davide Carnelli  
Complex Materials  
Department of Materials  
ETH Zürich  
Wolfgang-Pauli-Str. 10, 8093 Zürich  
Switzerland  
Phone: +41 44 633 0495  
Fax: +41 44 632 1101  
e-mail: [davide.carnelli@mat.ethz.ch](mailto:davide.carnelli@mat.ethz.ch)

## SUMMARY

Anisotropy is one of the most peculiar aspects of cortical bone mechanics; however, its anisotropic mechanical behavior should be treated only with strict relationship to the length scale of investigation.

In this study, we focus on quantifying the orientation and size dependence of the spatial mechanical modulation in individual secondary osteons of bovine cortical bone using nanoindentation. Tests were performed on the same osteonal structure in the axial (along the long bone axis) and transverse (normal to the long bone axis) directions along arrays going radially out from the Haversian canal at four different maximum depths on three secondary osteons.

Results clearly show a periodic pattern of stiffness with spatial distance across the osteon. The effect of length scale on lamellar bone anisotropy and the critical length at which homogenization of the mechanical properties occurs were determined. Further, a laminate-composite based analytical model was applied to the stiffness trends obtained at the highest spatial resolution to evaluate the elastic constants for a sub-layer of mineralized collagen fibrils within an osteonal lamella on the basis of the spatial arrangement of the fibrils.

The hierarchical arrangement of lamellar bone is found to be a major determinant for modulation of mechanical properties and anisotropic mechanical behavior of the tissue.

Keywords: hierarchical structure; anisotropy; length scale effect; nanoindentation; secondary osteons.

1 INTRODUCTION

Cortical bone is a heterogeneous, hierarchical composite material with important structural features spanning multiple length scales, each of which contributes to macroscopic biomechanical function [1-5]. At the microstructural level, both in humans and in many other large vertebrates, a particularly critical determinant of the mechanical properties of the whole tissue are concentric lamellar cylindrical structures called secondary osteons (Fig. 1 A-C) [6, 7].

The detailed lamellar structure within individual secondary osteons was interrogated via synchrotron X-ray texture measurements and consists of three-dimensional helicoids of mineralized collagen fibrils [6]. Transmission electron microscopy (TEM) [7-10] revealed that the mineralized collagen fibrils that make up one sub-layer of the lamellar unit have an internal crystalline structure. Within each lamella, which typically has a ~3-7  $\mu\text{m}$  thickness, the long axis of the collagen fibrils rotates from a direction roughly parallel to the osteonal axis at one lamellar boundary (referred to as “thick” sub-layers or sub-lamellae, ~2-4  $\mu\text{m}$  thick) to a direction approximately perpendicular to it at the opposite lamellar boundary (referred to as “thin” sub-layers or sub-lamellae, ~1-2  $\mu\text{m}$  thick).

The mechanical characterization of individual osteons was performed in tension, compression, and torsion [11-13], as well as with ultrasound [14]. Instrumented indentation was also applied to evaluate the elastic properties of lamellar bone within the osteonal structure along multiple orientations [15-17]. These studies identified anisotropic elasticity of individual osteons, where the axial direction was stiffer than the transverse direction with an anisotropic ratio (axial/transverse) of ~1.5, similar to the value found for macroscopic cortical bone [2, 3] and lower than the expected value for individual mineralized collagen fibrils (~2.0) [18].

Considering the hierarchical structural features of bone [6], different characteristic sizes which may also play functional roles in bone exist at different length scales [19-21]. In a recent study, Yao et al. [21] adopted AFM-based nanoindentation to identify a characteristic length scale of approximately 200 nm within one sub-layer of the lamellar unit; at a higher level, spatially-controlled nanoindentation experiments within individual osteons allowed Gupta et al. [19] to identify a larger characteristic length scale due to the periodicity of the osteonal lamellae, with thicker sub-lamellae of higher stiffness alternating with thinner sub-lamellae of lower stiffness. The spatial variation of indentation modulus within a lamella was attributed to the rotation of the inherently anisotropic collagen fibrils [19, 22] and variations in the mineral content [19]. Nevertheless, an experimentally validated analytical model that directly links the nanoscale rotational arrangements of collagen fibrils and the corresponding anisotropic elasticity is still missing.

In this study, we focus on quantifying the orientation and size dependence of the spatial mechanical modulation in individual secondary osteons of bovine cortical bone using nanoindentation. Experiments were carried out in two orthogonal orientations within the same individual osteon. Tests were performed at four different maximum penetration depths to study the effect of indentation area on mechanical modulation. An analytical model which assumes the inherent anisotropy of the mineralized collagen fibrils as well as their orientation was introduced to estimate the elastic constants of a sub-layer of mineralized collagen fibrils.

## 2 MATERIALS AND METHODS

In the following, the Haversian canal axis is referred to as the “Axial” direction (A), while the plane perpendicular to this axis is referred to as the “Transverse” direction ( $T_1$ ,  $T_2$ ). Similarly, the long axis of the mineralized collagen fibrils is herein referred to as the “Longitudinal” direction (L), while the plane perpendicular to this axis is referred to as the “Perpendicular”

direction ( $P_1$ ,  $P_2$ ). Thus,  $A$ ,  $T_1$ ,  $T_2$  represents a global coordinate system based on the whole secondary osteon; whereas,  $L$ ,  $P_1$ ,  $P_2$  represents a local coordinate system related to the mineralized collagen fibrils.

2.1 Sample preparation and characterization. Samples were kept under conditions close to the physiological one until the tests; to this purpose no alcohol dehydration, freezing, embedding, thermal drying, long-term storage in ambient conditions, or chemical fixation were used. Adult lamellar bone obtained from a 30-month old cow was harvested from between the tibial metaphysis and diaphysis. Approximately 5 mm cubic specimens were obtained by using a diamond-impregnated annular wafering saw (Isomet 5000, Buehler, Inc., Lake Bluff, IL, USA) running at 400–600 rpm under constant water irrigation. In order to expose the osteons' Haversian canal, the first two cuts were performed along the transverse direction and the second ones along the axial directions. The samples were then polished using a metallographic polishing wheel and adhesive papers with successively smaller  $Al_2O_3$  particle grit sizes. Samples were rinsed copiously with deionized (DI) water followed by ultrasonication in DI water between polishing intervals. The cutting and polishing procedures were performed the day after harvesting.

From optical (Nikon Eclipse L150, Fig. 1 A-B) and scanning electron microscopy (JEOL SEM 6320FV, Fig. 1 C), the average osteonal diameter was found to be  $\sim 200 \mu m$  and the average thickness of the first 4-5 individual lamellae around the Haversian canal is  $5.01 \pm 0.10 \mu m$ . Contact mode atomic force microscope (AFM, MFP-3D, Asylum Research, Inc., Santa Barbara, CA, USA) imaging was performed to assess the RMS surface roughness achieved with the polishing procedure, which was quantified as  $6.0 \pm 0.7 \text{ nm}$  on several  $2 \times 2 \mu m$  areas in different locations on the three osteonal structures.

Finally, samples were fixed into the groove of a home-built sample holder which allows for mechanical testing of the same osteonal structure in different directions with respect to the osteonal axis (Fig. 1 D-E).

2.2 Nanoindentation experiments. All instrumented indentation experiments were conducted in the osteonal region of cortical bone shortly after harvesting and over a short enough time period so that no significant modification of the sample state was ensured; to this purpose the statistical invariance of experimental data over time (the whole time span of the testing period) was checked (data not shown). The effect of hydration state was neglected at this stage, as the bone samples were tested in ambient conditions (20°C and 50% relative humidity). A Triboindenter (Hysitron, Inc., Minneapolis, MN, USA) was employed with a Berkovich diamond tip. The tip area function and machine compliance were calibrated on a fused silica reference sample by performing 100 indentations between 100 to 10000  $\mu\text{N}$  maximum forces [23].

Experiments were performed in displacement control along arrays going radially out from the Haversian canal edge to the external region of the osteon at four different maximum depths: 50, 100, 200 and 300 nm. The experimental procedure is detailed in Table 1. The displacement rates of the indentation experiments were 20 nm/s and 100 nm/s in the loading and unloading branches of the indentation curve, respectively. An automatic preliminary thermal drift correction was applied before each indentation. Preliminary investigations were performed to ensure that time-dependent effects were minimal (see [24] for further details). This experimental procedure was employed on three secondary osteons in both the axial and transverse directions (A and T<sub>1</sub>, respectively, in Fig. 1 A-E). A total of ~2000 indentations were carried out.

The Oliver-Pharr method [25] was adopted to obtain the indentation modulus  $M$  from the unloading portion of each test. An unloading segment range between 95% and 40% of maximum load was chosen for data fitting.

2.3 Empirical formulation for stiffness modulation. The oscillatory function:

$$M(r) = \frac{\Delta M}{2} \cdot \sin\left(\frac{2\pi r}{w} + c\right) + M_0 \tag{1}$$

was adopted to fit the stiffness modulation along the indentation paths. In Eq. (1),  $r$  is the radial position across the osteon,  $r=0$  being the Haversian canal inner edge;  $w$  is the mean value of the experimentally observed lamellar width (5.01  $\mu\text{m}$ );  $\Delta M$  is the oscillatory function amplitude;  $M_0$  is its mean value.

2.4 Anisotropic analytical models. The spatial modulation of stiffness at the lowest maximum indentation depth probed (50 nm) was fitted to an analytical model which assumes the inherent anisotropy of the mineralized collagen fibrils and allows for the evaluation of the effective stiffness of the sub-lamellae as a function of collagen fibril orientation. The orientation dependent uniaxial Young's modulus  $E$  of an individual sub-lamella was obtained by applying the rotation formula [19, 26, 27]:

$$E(\theta) = \left[ \frac{\cos^4(\theta)}{E_L} + \frac{\sin^4(\theta)}{E_P} + \left( \frac{1}{G_{LP}} - 2 \frac{\nu_{LP}}{E_L} \right) \cos^2(\theta) \sin^2(\theta) \right]^{-1} \tag{2}$$

where  $\theta$  is the angle between the long axis of the mineralized collagen fibrils (longitudinal direction, L) and the loading direction,  $E_L$  is the uniaxial Young's modulus along the mineralized collagen fibrils long axis direction (longitudinal direction, L),  $E_P$  is the uniaxial Young's modulus perpendicular to the mineralized collagen fibril axis (perpendicular directions,  $P_1$  and  $P_2$ ),  $G_{LP}$  is the shear modulus and  $\nu_{LP}$  is the Poisson's ratio. The model assumes that individual collagen fibrils and uniformly oriented planar layers of fibrils are transversely isotropic ( $P_1=P_2=P$ ) [28-30].

The uniaxial Young's moduli were directly estimated from the experimental nanoindentation loading-unloading curves by employing the analytical model for anisotropic elastic contact introduced by Delafargue and Ulm [31]. This model relates the indentation moduli of the mineralized collagen fibril sub-lamellae in the longitudinal (L) and perpendicular ( $P_1$ ,  $P_2$ ) directions to the material stiffness tensor coefficients for individual collagen fibril layers ( $C_{ijhk}=C_{ijhk}(E_L, E_P, G_{PL}, \nu_{LP}, \nu_{PP})$ ,  $\nu_{PP}$  being the Poisson's ratio in the isotropy plane). The model holds for transversely isotropic and orthotropic solids under rigid conical indentation along the three principal material symmetry directions. For a transversely isotropic material model, the indentation modulus  $M$  in the axis of symmetry direction (here named as direction 3, corresponding to the longitudinal collagen fibril axis direction L) is explicitly related to  $C_{ijhk}$  with the following expression:

$$M_3 = 2 \sqrt{\frac{C_{1111}C_{3333} - C_{1133}^2}{C_{1111}} \cdot \left( \frac{1}{C_{2323}} + \frac{2}{\sqrt{C_{1111}C_{3333} + C_{1133}}} \right)^{-1}} \quad (3)$$

For the indentation directions normal to the axis of symmetry (directions 1 and 2, corresponding to the perpendicular collagen fibril axes direction  $P_1=P_2=P$ ), the indentation moduli  $M_1, M_2$  are as follows:

$$M_1 = M_2 \approx \sqrt{\frac{C_{1111}^2 - C_{1122}^2}{C_{1111}} \cdot \left( \frac{C_{1111}}{C_{3333}} \right)^{1/2}} \cdot M_3 \quad (4)$$

The above formulae were applied at those indentation locations for which indentation direction is assumed to be aligned with a principal material direction (i.e. in the case of indentation of thick and thin sub-lamellae). Using the indentation moduli  $M_1$  and  $M_3$  calculated from nanoindentation data via the Oliver-Pharr method, Eqs. (3-4) were solved for  $E_L$  and  $E_P$ . The Poisson's ratios  $\nu_{LP}, \nu_{PP}$  were assumed according to literature data ([18], see Eq. (6)) and the shear modulus  $G_{LP}$  was related to the remaining parameters (see Eq. (6)).

For validation purposes, the Swadener-Pharr method [32] was employed to compute the indentation moduli  $M$  in all the directions of the space for a given stiffness tensor  $\mathbf{C}$ , as obtained from the solutions of Eqs. (2-4):

$$M = \frac{4\pi}{\int_0^{2\pi} \frac{\mathbf{B}^{-1}(\mathbf{t}(\gamma), \mathbf{C}) : [\mathbf{a}_3 \otimes \mathbf{a}_3]}{\sqrt{(a_1/a_2)\cos^2 \gamma + (a_1/a_2)\sin^2 \gamma}} d\gamma} \quad (5)$$

In this formulation,  $\mathbf{B}$  is the Barnett-Lothe tensor related to stiffness tensor  $\mathbf{C}$ ;  $(\mathbf{r}, \mathbf{s}, \mathbf{t})$  is an orthogonal reference system;  $(\mathbf{a}_1, \mathbf{a}_2, \mathbf{a}_3)$  is the indentation coordinate system;  $\gamma$  is the angle between the direction  $\mathbf{t}$  and the  $\mathbf{a}_1$  axis;  $a_1$  and  $a_2$  are the semi-axes lengths of the elliptical projected area of contact.

3 RESULTS

3.1 Mechanical modulation at the lamellar level. The average loading-unloading indentation curves obtained in the two orthogonal directions at the four maximum penetration depths are reported in Fig. 2. The curves show how the indentation response of the tissue depends on the global orientation direction (A vs. T). A good repeatability of the loading branch for increasing loads was obtained between tests at different maximum depth. The mean value and standard deviation of maximum load at 50, 100, 200, and 300 are 107 (±10) μN, 326 (±29) μN, 1004 (±69) μN, and 1984 (±104) μN, respectively, in the axial direction, and 110 (±19) μN, 263 (±29) μN, 648 (±77) μN, and 1354 (±218) μN, respectively, in the transverse direction. The corresponding COV (coefficient of variation, defined as the ratio between the standard deviation and the mean value) ranges between ~0.17 (at 50 nm maximum depth, transverse direction) and ~0.05 (at 300 nm maximum depth, axial direction). The tissue indentation modulus ranges from 26.24 (±1.68) GPa to 19.73 (±0.73) GPa in the axial direction and from 23.59 (±3.55) GPa to 15.39 (±1.04) GPa in the transverse

direction. The corresponding COV ranges between  $\sim 0.15$  (at 50 nm maximum depth, transverse direction) and  $\sim 0.04$  (at 300 nm maximum depth, axial direction).

The indentation modulus  $M$  shows a periodic alternating trend of stiffness with spatial distance radially across the osteon for both the axial (Fig. 3) and transverse (Fig. 4) directions, consistent with results reported in [19]. The coefficient of determination ( $R^2$ ) for fits of the experimental data (Figs. 3-4) to Eq. (1) ranged between 0.61 and 0.01. Higher correlations were found for data taken at the smaller depths (50 nm), while smaller values corresponded to indentations carried out at 300 nm depths in both directions. All the obtained  $R^2$  values are reported in the caption of Figs. 3-4. Further, a power analysis has been carried out on the data of Figs. 3-4. A statistically significant difference (one-way ANOVA,  $p < 0.001$ ) was found between the peaks and the valleys of the modulation at 50 and 100 nm maximum depth in both the axial and transverse direction, as well as for the 200 nm, axial direction experiments ( $p < 0.05$ ). Instead, no statistically significant difference ( $p > 0.05$ ) was found at 200 nm maximum depth in the transverse direction and at 300 nm maximum depth.

The mean value,  $M_0$ , and the amplitude of the modulation,  $\Delta M$ , depend on maximum depth and orientation of the indentation tests (Fig. 5). The mean values  $M_0$  show the tissue to be stiffer when loaded in the axial direction compared to the transverse direction (Fig. 5A): indeed, anisotropy ratios, calculated as axial vs. transverse indentation moduli mean values, vary between  $\sim 1.1$  at lower maximum indentation depths (50 and 100 nm) to  $\sim 1.3$  at higher maximum indentation depths (200 and 300 nm). Simultaneously, the spatial modulation of the mechanical properties is higher in the transverse compared to the axial direction (i.e. higher  $\Delta M$ , Fig. 5B). A decrease in the indentation moduli mean values is observed between 50 and 200 nm maximum depths, this decay being more pronounced in the transverse ( $\sim 35\%$ ) than in the axial ( $\sim 22\%$ ) direction. Instead, no statistically significant difference (one-way ANOVA,  $p > 0.05$ ,  $n=9$ ) is noticeable within the same direction between 200 and 300 nm (Fig.

5A). The amplitude of the stiffness modulation (Fig. 5B) decreases with the indentation depth as well. The transverse amplitude is approximately two times higher than the axial at 50 nm indentation depth, while the trends in the two directions are similar beyond 100 nm depth: indeed, at higher indentation depths (200 and 300 nm), the amplitude values in both directions vanish and the difference between the amplitude values becomes negligible, as the two datasets show no statistically significant difference ( $p>0.05$ ,  $n=9$ ).

3.2 Estimation of  $E_L$ ,  $E_P$  and  $E(\theta)$  from the anisotropic analytical models. It is expected that carrying out indentations spatially from the Haversian canal edge to the osteonal external boundary will result in the angle  $\theta$  continuously changing along the radial path due to the spiral twisting of the mineralized collagen fibrils within a single lamella.  $E_L$  and  $E_P$  were estimated from indentation data at the lowest maximum indentation depth (50 nm, where both the spatial and depth resolution of the experiments were the highest, Figs. 3A-4A) using the Delafargue and Ulm model [31]. Since this approach is valid only in the principal material symmetry directions, the analysis was carried out at spatial locations across the osteon where the indentation loading axis was parallel and perpendicular to the mineralized collagen fibrils long axis, that is at the 9 different points  $r_i$  (with  $r_i=0, 2.5, 5, 7.5, 10, 12.5, 15, 17.5$  and  $20 \mu\text{m}$  radial distances from the Haversian canal edge) corresponding to the peaks and valleys of the stiffness modulation in the axial and transverse directions (Figs. 3A-4A). Thus, the indentation moduli  $M_A(r_i)$  and  $M_T(r_i)$  estimated from the Oliver-Pharr method represent the left-hand side of the system of Eqs. (3-4). In order to simultaneously calculate the uniaxial elastic moduli  $E_L(r_i)$  and  $E_P(r_i)$ , the three remaining material constants  $\nu_{PP}(r_i)$ ,  $\nu_{LP}(r_i)$  and  $G_{LP}(r_i)$  were set to:

$$\nu_{PP}(r_i) = 0.358; \quad \nu_{LP}(r_i) = 0.315; \quad G_{LP}(r_i) = \frac{E_L(r_i) + E_P(r_i)}{2} \cdot \frac{1}{2 \cdot \left( 1 + \frac{\nu_{LP}(r_i) + \nu_{PL}(r_i)}{2} \right)} \quad (6)$$

Here,  $\nu_{pp}(r_i)$  and  $\nu_{LP}(r_i)$  are average values from literature ([18], see Table 3) and refer to the mechanical properties of a single sub-lamella. This procedure was applied to the couples of indentation moduli  $M_A(r_i)$  and  $M_T(r_i)$ , enabling the identification of the corresponding couples of uniaxial elastic moduli  $E_L(r_i)$  and  $E_p(r_i)$  reported in Fig. 6A-B (bars).

The analytical model in Eq. (2) was then adopted to calculate  $E(\theta)$  in the axial and transverse directions (Figs. 6A-B, sinusoidal curves), thus allowing the prediction of the stiffness at any arbitrary angle with respect to the fibril axis for the two experimental trends. In both cases, the Poisson's ratio  $\nu_{LP}$  was set to the corresponding literature values for a sub-layer in an osteonal lamella found by Yoon and Cowin ([18], see Table 3); also, the periodicity of the modulation was set to the experimentally observed lamellar width (5.01  $\mu\text{m}$ ). Results of this fitting are provided in Table 2. The small discrepancy ( $\sim 6\%$ ) in  $E_L$  between the axial and transverse directions means that the mineralized collagen fibrils belonging to the thick and thin sub-lamellae maintain similar longitudinal mechanical properties.  $E_p$  exhibited a much higher discrepancy between axial and transverse direction ( $\sim 23\%$ ) indicating that the transverse properties of the mineralized collagen fibrils are different in the thick and thin sub-lamellae.

**3.3 Elastic constants for a sub-layer within an osteonal lamella.** A set of orthotropic elastic parameters for a mineralized collagen fibrils sub-layer was inferred from the previous fittings by properly merging the two datasets reported in Table 2. In the proposed set of elastic parameters (Table 3), the uniaxial Young's modulus  $E_L$  corresponds to the mean value of the Young's moduli evaluated along the fibrils long axis in thin and thick layers; instead, uniaxial Young's moduli  $E_{P1}$  and  $E_{P2}$ , as well as the shear moduli  $G_{LP1}$  and  $G_{LP2}$ , are directly obtained from the previous fittings. The remaining entries of the stiffness tensor, i.e. the shear modulus and the Poisson's ratio in the  $P_1$ - $P_2$  plane,  $G_{P1P2}$  and  $\nu_{P1P2}$ , were taken from literature

([18], see Table 3). For comparison purposes, the set of orthotropic elastic for a sub-layer in an osteonal lamella obtained by Yoon and Cowin [18] are included in Table 3.

3.4 *Validation of the experimental and analytical procedures.* In order to validate the above procedure, the indentation moduli trends in the axial and transverse directions at 50 nm depth were calculated through the Swadener-Pharr method [32] using the set of elastic parameters reported in Table 2 (transversely isotropic model) and in Table 3 (orthotropic model). The indentation moduli are computed using 5° spacing for  $\theta$ , corresponding to ~140 nm spacing in the radial paths. The computed values, compared to the experimental measures obtained at 50 nm maximum depth (Figs. 3A-4A) and the fitting to the oscillatory function of Eq. (1), are shown in Fig. 7. Both material models agree reasonably well with the experimental values, as evidenced by the coefficients of determination  $R^2$  (reported in Fig. 7 caption) ranging between 0.59 and 0.62.

Results from the application of the Swadener-Pharr method are also presented in Tables 4-5, where the indentation moduli mean value and amplitude of the modulation calculated with the oscillatory function best fitting the data (see Eq. (1)) are compared to the computed mean value and amplitude of the oscillatory trends (dotted lines in Fig. 7). The percentage differences between the experimental and the computed indentation values are lower for the orthotropic elastic behavior (below 5%) than the transversely isotropic behavior, where differences up to ~20% were found. The two pieces of evidence above - i.e. the fact that the coefficient of determination  $R^2$  associated to the Swadener-Pharr prediction with an orthotropic material model is similar to the  $R^2$  values obtained via Eq. (1), and the low discrepancy in terms of indentation moduli mean value and amplitude of the modulation between the experimental and the computed data for and orthotropic model – support both the reliability of the elastic parameters obtained through application of Eq. (2) to the data and the

assumption of orthotropy to model the elastic mechanical behavior of a sub-layer of mineralized collagen fibrils within an osteonal lamella.

#### 4 DISCUSSION

The aim of the study was to determine the orientation and size dependent mechanical properties of individual secondary osteons in cortical bone, as well as to investigate the way the constituents' anisotropy and their arrangement in the hierarchical structure concur in the development of the anisotropic mechanical behavior of the tissue. Indentation experiments at different maximum depths showed a periodic alternating of stiffer layers with less stiff layers in which the indentation modulus mean values as well as the amplitude of the modulation depend on maximum depth and orientation of the indentation tests. A characteristic length due to the periodicity of the osteonal lamellae was quantified. Further, the elastic constants for a sub-layer of mineralized collagen fibrils within an osteonal lamella were identified from the indentation moduli by applying an analytical model which assumes inherent anisotropy of the mineralized collagen fibrils as well as their spatial arrangement.

The smallest experimental characteristic length probed (50 nm maximum depth, ~400 nm contact diameter) is comparable to the size of a few mineralized collagen fibrils and allowed the evaluation of the mechanical properties of a single sub-layer of fibrils in the lamellar structure; whereas, the largest experimental characteristic length sampled (300 nm maximum depth, ~2.0  $\mu\text{m}$  contact diameter) may accommodate ~10 to 20 bunches of collagen fibrils oriented along multiple directions and, thus, involves multiple sub-layers, whose thickness can vary between few hundreds of nanometers to a couple of microns [22, 33-35]. These investigations enabled the identification of a decrease in the values of indentation moduli with the penetration depth (Fig. 5A) which indicates a possible size effect in the mechanical properties of cortical bone tissue. At the same time, decreasing values of

amplitude  $\Delta M$  (Fig. 5B) indicate that the indentation experiment is involving a sufficient amount of tissue volume such that homogenized material properties are sensed by the indentation probe. The stabilization of  $M_0$  and the decay to a negligible value of  $\Delta M$  occurs at approximately the same length scale. This suggests that the homogenization process has completely developed at approximately 300 nm maximum depth, corresponding to a  $\sim 2 \mu\text{m}$  contact diameter between the tissue and the indenter.

Homogenization arguments alone are not able to fully justify the pronounced decay of the indentation moduli with the penetration depth achieved with the experimental tests, quantifiable in  $\sim 24\%$  and  $\sim 34\%$  reductions in the axial and transverse directions, respectively. Instead, the decrease in indentation modulus with indentation depth may be explained by considering peculiar deformation and failure mechanisms of bone tissue at the nanostructural level, such as shear transfer between mineral particles via intermediate ductile organic layers [36], slippage at the collagen–mineral interface [37], phase transformation of the mineral phase [38], and sacrificial bond disruption between fibrils [39]. In particular, Gupta and coworkers [40, 41] showed that critical interfacial shear strength between the fibril and the interfibrillar matrix layer is exceeded when the bone is compressed above the yield point. When this happens, the matrix flows past the fibrils, resulting in frictional losses and debonding of the fibrils and extrafibrillar matrix. A further evidence for this mechanism is achieved considering a single loading-unloading cycle of bone [41], as when a bone sample is relaxed after being deformed beyond the yield point, irreversible deformations develop at the tissue level but not at the fibril level. If we compare the loading and unloading stiffnesses at the tissue level, damage induced decrease in the tissue Young’s modulus occurs: this decay, quantified as  $\sim 20\text{--}25\%$ , is consistent with the progressive diminishing of the stiffness mean value while increasing the maximum depth evidenced in the present work. Moreover, as the deformation mechanisms mentioned above contribute in determining a loss of integrity of the

1  
2  
3 tissue, they can be considered as damage phenomena that cause a progressive degradation of  
4  
5 material continuity; we speculate that a damage model can phenomenologically represents  
6  
7 the overall tissue response subject to nanoindentation. Recently, a numerical study performed  
8  
9 by our group [42] was devoted to the investigation of the role played by damage mechanics in  
10  
11 the nanoindentation of osteonal lamellar bone and we showed that damage models can  
12  
13 predict the loss in mechanical properties obtained in the experiments.  
14  
15

16  
17 The results of this work show that the stiffness modulation of the tissue is consistent  
18  
19 with anisotropic fibrillar layers with a specific crystal orientation. Indeed, based on the  
20  
21 difference of the elastic moduli in the directions perpendicular to the fibril ( $E_P$ , see Table 2)  
22  
23 between the thick and this sub-lamellae, it can be speculated that the mineral platelets have an  
24  
25 intrinsic orientation that could play a role in determining the mechanical properties normal to  
26  
27 the fibrils long axis. This observation would agree with the rotated plywood model  
28  
29 introduced by Weiner et al. [33, 34], where collagen fibrils are rotated not only with respect  
30  
31 to the lamellar boundary but also around their own axis (Fig. 8), as the mechanical properties  
32  
33 obtained for a sub-layer can be explained by the azimuthal rotation of the fibrils around the  
34  
35 longitudinal axis  $L$ , which changes the crystal orientation. A further evidence that the  
36  
37 hydroxyapatite crystals strongly influences the elastic properties of the mineralized collagen  
38  
39 fibrils along different directions is provided by Rho et al. [43], who studied intramuscular  
40  
41 herring bones where mineralized collagen fibrils have a single orientation with a variation in  
42  
43 mineralization along the length. Results clearly showed that the anisotropy ratio is influenced  
44  
45 by the mineralization, as it drops from  $\sim 2.1$  in the fully mineralized region to  $\sim 1.1$  in areas at  
46  
47 the earliest stage of mineralization. In this case, the presence of the mineral crystals seems to  
48  
49 be the main aspect responsible for the difference in the elastic properties along different  
50  
51 directions.  
52  
53  
54  
55  
56  
57  
58  
59  
60

As already said in the materials and methods section, the bone samples were tested in ambient conditions. Although samples still retain a significant degree of hydration in this condition, in general an artificial increase in stiffness and reduction in ductility compared to the native state could results. However, Hengsberger et al. [44] adopted instrumented indentation to compare dry and wet samples at different length scales, which are comparable to the ones investigated here. Basically, what they found is that: (i) thick lamellae exhibited a significant decrease in indentation modulus with increasing indentation depth, as reported in this study; (ii) the comparative trends of indentation depth and lamella type were similar for dry and physiological conditions. Thus the effect of testing dry instead of wet samples seems the same at multiple length scales. Therefore, relative modulations in mechanical properties are expected to remain valid, as well as the comparison between the mechanical properties at the different experimental characteristic length probed and along different directions. Anyway, future developments will consider the application of the present experimental-analytical procedure to tests in conditions closer to the physiological.

**5 CONCLUSION**

In this work, the hierarchical arrangement of lamellar bone was found to be a major determinant for modulation of mechanical properties and anisotropic mechanical behavior of the tissue. More in detail:

- the size effect on lamellar bone anisotropic mechanical behavior, evidenced by the decline of indentation modulus versus probe size, and the critical length at which homogenization of the mechanical properties occurs were determined by measuring the spatial modulation of indentation response;
- by employing a laminate-composite based analytical model, the elastic constants for a sub-layer of mineralized collagen fibrils within an osteonal lamella were determined on

the basis of their spatial arrangements and were validated through direct comparison of the experimental indentation moduli and the predicted ones computed by the Swadener-Pharr model;

The structural complexity of bone tissue requires that the assessment of its mechanical properties involves multiple hierarchical levels, from the macroscopic scale down to the micro and nanostructural level till the most basic components. Understanding structure-property relationships and the effects of structural features on the biomechanical properties of bone would enable not only the development of more accurate models for analysis of implants and potential bone-replacement materials, but also the progress in designing bio-inspired structural materials which take advantage of the mechanical design principles found in nature. These latter topics undoubtedly represent fascinating long-term scientific goals in the materials science and engineering field.

## ACKNOWLEDGMENTS

The authors would like to thank the MIT-Italy Program for supporting the research and the Progetto Rocca for supporting Davide Carnelli's scholarship at the MIT. The DMSE Nanomechanical Technology Laboratory and the Institute for Soldier Nanotechnologies (ISN) at the MIT are gratefully acknowledged for use of equipment and facilities. MD acknowledges support by the ONR Grant N00014-08-1-0510, and by the Advanced Materials for Micro and Nano Systems Programme of the Singapore-MIT Alliance (SMA).

REFERENCES

1. Weiner, S. & Wagner, H. D. 1998 The material bone: structure mechanical function relations. *Annu. Rev. Mater. Sci.* **28**, 271-298. (DOI 10.1146/annurev.matsci.28.1.271)

2. Currey, J. D. 2002 *Bones: structure and mechanics*. Princeton, NJ: Princeton University Press.

3. Cowin, S. C. 2001 *Bone mechanics handbook*. Boca Raton, FL: CRC Press Inc.

4. Currey, J. D. 1984 *The mechanical adaptations of bones*. Princeton, NJ: Princeton University Press.

5. Rho, J. Y., Kuhn-Spearing, L. & Zioupos, P., 1998 Mechanical properties and the hierarchical structure of bone. *Med. Eng. Phys.*, **20**, 92-102. (DOI 10.1016/S1350-4533(98)00007-1)

6. Fratzl, P. & Weinkamer, R. 2007 Nature's hierarchical materials. *Progress Mater. Sci.* **52**, 1263-1334. (DOI 10.1016/j.pmatsci.2007.06.001)

7. Fratzl, P., Gupta, H. S., Paschalis, E. P. & Roschger, P. 2004 Structure and mechanical quality of the collagen-mineral nano-composite in bone. *J. Mater. Chem.* **14**, 2115-2123. (DOI 10.1039/B402005G)

8. Fratzl, P. & Gupta, H. S. 2007 *Nanoscale mechanisms of bone deformation and fracture*. Weinheim: Wiley-VCH Verlag GmbH.

9. Wagermaier, W., Gupta, H.S., Gourrier, A., Burghammer, M., Roschger, P. & Fratzl, P. 2006 Spiral twisting of fiber orientation inside bone lamellae. *Biointerph.* **1**, 1-5. (DOI 10.1116/1.2178386)

10. Wagermaier, W., Gupta, H. S., Gourrier, A., Paris, O., Roschger, P., Burghammer, M., Riekel, C. & Fratzl P. 2007 Scanning texture analysis of lamellar bone using microbeam synchrotron x-ray radiation. *J. Appl. Crystall.* **40**, 115-120. (DOI 10.1107/S0021889806044888)

11. Reilly, D. T. & Burstein, A. H. 1975 The elastic and ultimate properties of compact bone tissue. *J. Biomech.* **6**, 393-396. (DOI 10.1016/0021-9290(75)90075-5)
12. Ascenzi, A., Baschieri, P. & Benvenuti, A. 1994 The torsional properties of single selected osteons. *J. Biomech.* **27**, 875-884. (DOI 10.1016/0021-9290(94)90260-7)
13. Ascenzi, A., Ascenzi, M. G., Benvenuti, A. & Mango, F. 1997 Pinching in longitudinal and alternate osteons during cyclic loading. *J. Biomech.* **30**, 689-695. (10.1016/S0021-9290(97)00002-X)
14. Rho, J. Y. 1996 An ultrasonic method for measuring the elastic properties of human tibial cortical and cancellous bone. *Ultrasonics* **34**, 777-783. (DOI 10.1016/S0041-624X(96)00078-9)
15. Fan, Z., Swadener, J. G., Rho, J. Y., Roy, M. E. & Pharr, G. M. 2002 Anisotropic properties of human tibial cortical bone as measured by nanoindentation. *J. Orthop. Res.* **20**, 806-810. (DOI 10.1016/S0736-0266(01)00186-3)
16. Rho, J. Y., Currey, J. D., Zioupos, P. & Pharr, G. M. 2001 The anisotropic young's modulus of equine secondary osteons and interstitial bone determined by nanoindentation. *J. Exp. Biol.* **204**, 1775-1781.
17. Franzoso, G. & Zysset, P.K. 2009 Elastic anisotropy of human cortical bone secondary osteons measured by nanoindentation. *J. Biomech. Eng.* **131**, 021001.1-021001.11.
18. Yoon, Y. J. & Cowin, S. C. 2008 The estimated elastic constants for a single bone osteonal lamella. *Biomech. Model. Mechanobiol.* **7**, 1-11. (DOI 10.1007/s10237-006-0072-8)
19. Gupta, H. S., Stachewicz, U., Wagermaier, W., Roschger, P., Wagner, H. D. & Fratzl, P. 2006 Mechanical modulation at the lamellar level in osteonal bone. *J. Mater. Res.* **21**, 1913-1921. (DOI 10.1557/jmr.2006.0234)
20. Kasiri, S. & Taylor, D. 2008 A critical distance study of stress concentrations in bone. *J. Biomech.* **41**, 603-609. (DOI 10.1016/j.jbiomech.2007.10.003)

21. Yao, H., Dao, M., Carnelli, D., Tai, K. & Ortiz, C. 2011 Size-dependent heterogeneity benefits the mechanical performance of bone. *J. Mech. Phys. Sol.* **59**, 64-74. (DOI 10.1016/j.jmps.2010.09.012)

22. Hofmann, T., Heyroth, F., Meinhard, H., Franzel, W. & Raum, K. 2006 Assessment of composition and anisotropic elastic properties of secondary osteon lamellae. *J. Biomech.* **39**, 2282-2294. (DOI 10.1016/j.jbiomech.2005.07.009)

23. Oliver, W. C. & Pharr, G. M. 2004 Measurement of hardness and elastic modulus by instrumented indentation: Advances in understanding and refinements to methodology. *J. Mater. Res.* **19**, 3-20. (DOI 10.1557/jmr.2004.19.1.3)

24. Tai, K., Qi, H. J. & Ortiz, C. 2005 Effect of mineral content on the nanoindentation properties and nanoscale deformation mechanisms of bovine tibial cortical bone. *J. Mater. Sci.: Mater. Med.* **16**, 947-959. (DOI 10.1007/s10856-005-4429-9)

25. Oliver, W. C. & Pharr, G. M. 1992 An improved technique for determining hardness and elastic modulus using load and displacement sensing indentation experiments. *J. Mater. Res.* **7**, 1564-1583. (DOI 10.1557/JMR.1992.1564)

26. Currey, J. D. 1969 The relationship between the stiffness and the mineral content of bone. *J. Biomech.* **2**, 477-480. (DOI 10.1016/0021-9290(69)90023-2)

27. Seto, J., Gupta, H. S., Zaslansky, P., Wagner, H. D. & Fratzl, P. 2008 Tough lessons from bone: extreme mechanical anisotropy at the mesoscale. *Adv. Funct. Mater.* **18**, 1905-1911. (DOI 10.1002/adfm.200800214)

28. Fritsch, A. & Hellmich, C. 2007 Universal microstructural patterns in cortical and trabecular, extracellular and extravascular bone materials: micromechanics-based prediction of anisotropic elasticity. *J. Theoret. Biol.* **244**, 597-620. (DOI 10.1016/j.jtbi.2006.09.013)

29. Hellmich, C. & Ulm, F. J. 2002 Are mineralized tissues open crystal foams reinforced by crosslinked collagen?-some energy arguments. *J. Biomech.* **35**, 1199-1212. (DOI 10.1016/S0021-9290(02)00080-5)
30. Hellmich, C., Barthélémy, J-F. & Dormieux, L. 2004 Mineral-collagen interactions in elasticity of bone ultrastructure-a continuum micromechanics approach. *Eur. J. Mech. - A/Solids* **23**, 783-810. (DOI 10.1016/j.euromechsol.2004.05.004)
31. Delafargue, A. & Ulm, F.J. 2004 Explicit approximations of the indentation modulus of elastically orthotropic solids for conical indenters. *Int. J. Solids Struct.* **41**, 7351-7360. (DOI 10.1016/j.ijsolstr.2004.06.019)
32. Swadener, J. G. & Pharr, G.M. 2001 Indentation of elastically anisotropic half-spaces by cones and parabolas of revolution. *Phil. Mag. A* **81**, 447-466. (DOI 10.1080/01418610108214314)
33. Weiner, S., Arad, T., Sabanay, I. & Traub, W. 1997 Rotated plywood structure of primary lamellar bone in the rat: orientations of the collagen fibril arrays. *Bone* **20**, 509-514. (DOI 10.1016/S8756-3282(97)00053-7)
34. Weiner, S., Traub, W. & Wagner, H. D. 1999 Lamellar bone: structure-function relations. *J. Struct. Biol.* **126**, 241-255. (DOI 10.1006/jsbi.1999.4107)
35. Akiva, U., Wagner, H. D. & Weiner, S. 1998 Modelling the three-dimensional elastic constants of parallel-fibred and lamellar bone. *J. Mater. Sci.* **33**, 1497-1509. (DOI 10.1023/A:1004303926771)
36. Jager, I. & Fratzl, P. 2000 Mineralized collagen fibrils: a mechanical model with a staggered arrangement of mineral particles. *Biophys. J.* **79**, 1737-1746. (DOI 10.1016/S0006-3495(00)76426-5)

37. Mercer, C., He, M. Y., Wang, R. & Evans, A.G. 2006 Mechanisms governing the inelastic deformation of cortical bone and application to trabecular bone. *Acta Bio.* **2**, 59-68. (DOI 10.1016/j.actbio.2005.08.004)
38. Carden, A., Rajachar, R.M., Morris, M.D. & Kohn, D. H. 2003 Ultrastructural changes accompanying the mechanical deformation of bone tissue: a raman imaging study. *Calcif. Tissue Int.* **72**, 166-175. (DOI 10.1007/s00223-002-1039-0)
39. Fantner, G., Hassenkam, T., Kindt, J. H., Weaver, J. C., Birkedal, H., Pechenik, L., Cutroni, J. A., Cidade, G. A. G., Stucky, G. D., Morse, D. E. & Hansma, P.K. 2005 Sacrificial bonds and hidden length dissipate energy as mineralized fibrils separate during bone fracture. *Nat. Mater.* **4**, 612-616. (DOI 10.1038/nmat1428)
40. Gupta, H. S., Wagermaier, W., Zickler, G. A., Aroush, D. R. B., Funari, S. S., Roschger, P., Wagner, H. D. & Fratzl, P. 2005 Nanoscale deformation mechanisms in bone. *Nano Lett.* **5**, 2108-2111. (DOI 10.1021/nl051584b)
41. Gupta, H. S., Wagermaier, W., Zickler, G. A., Hartmann, J., Funari, S. S., Roschger, P., Wagner, H.D. & Fratzl, P. 2006 Fibrillar level fracture in bone beyond the yield point. *Int. J. Fracture* **139**, 425-436. (DOI 10.1007/s10704-006-6635-y)
42. Lucchini, R., Carnelli, D., Ponzoni, M., Bertarelli, E., Gastaldi, D. & Vena, P. 2011 Role of damage mechanics in nanoindentation of lamellar bone at multiple sizes: experiments and numerical modeling. *J. Mech. Behav. Biomed. Mater.* **4**, 1852-1863. (DOI 10.1016/j.jmbbm.2011.06.002)
43. Rho, J. Y., Mishra, S. R., Chung, K., Bai, J. & Pharr, G. M. 2001 Relationship between ultrastructure and the nanoindentation properties of intramuscular herring bones. *Annals Biomed. Eng.* **29**, 1082-1088. (DOI 10.1114/1.1424913)

- 1  
2  
3 44. Hengsberger, S., Kulik, A. & Zysset, P. 2002 Nanoindentation discriminates the  
4 elastic properties of individual human bone lamellae under dry and physiological conditions.  
5  
6  
7 *Bone* **30**, 178-184. (DOI 10.1016/S8756-3282(01)00624-X)  
8  
9  
10  
11  
12  
13  
14  
15  
16  
17  
18  
19  
20  
21  
22  
23  
24  
25  
26  
27  
28  
29  
30  
31  
32  
33  
34  
35  
36  
37  
38  
39  
40  
41  
42  
43  
44  
45  
46  
47  
48  
49  
50  
51  
52  
53  
54  
55  
56  
57  
58  
59  
60

For Review Only

FIGURES

**Figure 1.** (A) Optical microscopy image of osteonal bovine bone tissue parallel to the osteonal axis (axial direction). (B) Optical microscopy image of osteonal bovine bone tissue normal to the osteonal axis (transverse direction). (C) Scanning electron microscopy image of a region surrounding an individual osteon parallel to the osteonal axis. (D) Home built sample stage enabling the testing of two orthogonal orientations within the same osteon. (E) Illustration of the indentation test directions ( $A$  and  $T_1$ ) with respect to the osteonal microstructure (in red).

**Figure 2.** Averaged load vs. penetration depth plots in the axial (A) and transverse (B) directions at the four tested maximum depths. Error bars are  $\pm$  one standard deviation calculated at 50% of the maximum load during the unloading curve ( $n=363$  for 50 nm maximum depth tests,  $n=273$  for 100 nm maximum depth tests,  $n=189$  for 200 and 300 nm maximum depth tests).

**Figure 3.** Spatial dependence of indentation modulus at 50 (A), 100 (B), 200 (C) and 300 (D) nm maximum penetration depth for axial experiments (parallel to the osteonal axis). Radial distance ( $r$ ) begins at the Haversian canal edge. Each data point represents the mean value and standard deviation of a total of  $n=9$  measurements. The fitting to the oscillatory function of Eq. (1) is shown in each plot (dashed line). The coefficient of determination ( $R^2$ ) values are 0.60 (A), 0.59 (B), 0.59 (C), and 0.01 (D). Note ordinate does not start at zero.

**Figure 4.** Spatial dependence of indentation modulus at 50 (A), 100 (B), 200 (C) and 300 (D) nm maximum penetration depth for transverse experiments (normal to the osteonal axis). Radial distance ( $r$ ) begins at the Haversian canal edge. Each data point represents the mean

value and standard deviation of a total of  $n=9$  measurements. The fitting to the oscillatory function of Eq. (1) is shown in each plot (dashed line). The coefficient of determination ( $R^2$ ) values are 0.61 (A), 0.58 (B), 0.61 (C), and 0.01 (D). Note ordinate does not start at zero.

**Figure 5.** Indentation modulus mean value (A) and amplitude (B) trends with respect to penetration depth in the axial and transverse directions calculated from Eq. (1). Standard deviations refer to  $n=9$  measurements.

**Figure 6.** Spatial modulation (bars) of the uniaxial elastic moduli  $E$  obtained by using the Delafargue-Ulm approach [31] at 50 nm maximum penetration depth in the axial (A) and transverse (B) directions. Maxima correspond to  $E_L$  (longitudinal to collagen fibril long axis) and minima correspond to  $E_P$  (transverse to collagen fibril long axis). Standard deviations refer to  $n=9$  measurements. Fitting with the analytical model in Eq. (2) is also shown: the fitting results, together with the coefficient of determination values  $R^2$ , are reported in Table 2. Note ordinate does not start at zero.

**Figure 7.** Comparison between the indentation moduli trends obtained experimentally (bars) and the ones computed with the Swadener-Pharr method [32] (dots) with a  $\sim 140$  nm spacing in the axial (A) and transverse (B) directions. The fitting to the oscillatory function of Eq. (1) (dashed line) is shown as well. The input parameters for the Swadener-Pharr method are reported in Tables 2-3 for transversely isotropic (TI) and orthotropic (ORTH) material models, respectively. In the axial direction (A), the coefficient of determination  $R^2$  values are 0.59 and 0.60 for the transversely isotropic and orthotropic model, respectively; whereas, in the transverse direction (B),  $R^2$  values are 0.62 and 0.61 for the transversely isotropic and orthotropic model, respectively. Note ordinate does not start at zero.

**Figure 8.** Schematic illustration of the organization of mineralized collagen fibrils and the plate-shaped mineral crystals within the fibrils in a lamellar unit of osteonal bone according to the rotated plywood model introduced by Weiner et al. [33, 34]. The three local orthogonal reference axes labeled  $L$ ,  $P_1$  and  $P_2$  (relative to the axis of an individual mineralized collagen fibril) are provided. The three global orthogonal reference axes  $A$ ,  $T_1$  and  $T_2$  (relative to the osteonal axis) are provided too. Not drawn to scale.

## TABLES

**Table 1.** Summary of the indentation tests carried out in this work. The procedure explained below has been performed in both the axial (A) and transverse ( $T_1$ ) directions on three secondary osteons.

Number of Indentations rows×columns	Maximum depth	Spacing
41×3	50 nm	0.5 $\mu\text{m}$
31×3	100 nm	1 $\mu\text{m}$
21×3	200 nm	2 $\mu\text{m}$
21×3	300 nm	3 $\mu\text{m}$

**Table 2.** Results of fitting with Eq. (2) [19, 26, 27] independently applied to the 50 nm maximum depth data in terms of uniaxial elastic moduli  $E$  (Fig. 7) in the axial and transverse directions. The  $\nu_{LP}$  values (bold typed) were assumed from [18] to perform the fitting. The coefficient of determination  $R^2$  is given in the last column.

Indentation Direction	$E_L$ [GPa]	$E_P$ [GPa]	$G_{LP}$ [GPa]	$\nu_{LP}$ [-]	$R^2$ [-]
Axial	27.70	22.60	9.26	<b>0.301</b>	0.88
Transverse	26.17	17.98	8.16	<b>0.330</b>	0.86

**Table 3.** Set of orthotropic elastic parameters for a sub-layer of mineralized collagen fibrils within an osteonal lamella, inferred by properly merging the two datasets in the axial and transverse directions reported in Table 2. The  $G_{PIP2}$ ,  $\nu_{PIP2}$ ,  $\nu_{LP1}$ , and  $\nu_{LP2}$  parameters (bold typed) were assumed from [18]. For comparison purposes, the set of orthotropic elastic parameters for one sub-layer of the lamellar unit obtained by Yoon and Cowin [18] is reported also. The relationships  $E_L > E_{P2} > E_{P1}$  and  $\nu_{P2P1} > \nu_{P2L} > \nu_{P1L}$  are maintained, as well as  $G_{LP2} > G_{LP1}$ .

	$E_{P1}$ [GPa]	$E_{P2}$ [GPa]	$E_L$ [GPa]	$G_{PIP2}$ [GPa]	$G_{LP1}$ [GPa]	$G_{LP2}$ [GPa]	$\nu_{PIP2}$ [-]	$\nu_{P2P1}$ [-]	$\nu_{P1L}$ [-]	$\nu_{P2L}$ [-]	$\nu_{LP1}$ [-]	$\nu_{LP2}$ [-]
Present work	17.98	22.60	26.94	<b>7.2</b>	8.16	9.26	<b>0.334</b>	0.420	0.220	0.253	<b>0.330</b>	<b>0.301</b>
Yoon, Cowin	16.40	18.07	22.80	7.2	7.1	8.4	0.334	0.381	0.237	0.247	0.330	0.301

**Table 4.** Comparison between the indentation moduli mean value and amplitude of the modulation calculated with the oscillatory function in Eq. (1) and computed by the Swadener-Pharr method [32] in the axial and transverse direction. Percentage discrepancies are calculated as  $e_{M0} = |M_0^{COM} - M_0^{EQ.I}| / M_0^{EQ.I}$  and  $e_{\Delta M} = |\Delta M^{COM} - \Delta M^{EQ.I}| / \Delta M^{EQ.I}$ . The transversely isotropic material model is used.

Indentation Direction	$M_0^{EQ.I}$ [GPa]	$M_0^{COM}$ [GPa]	$\Delta M^{EQ.I}$ [GPa]	$\Delta M^{COM}$ [GPa]	$e_{M0}$ %	$e_{\Delta M}$ %
Axial	26.19	27.00	2.48	2.97	3.07	19.76
Transverse	23.56	23.15	5.53	5.01	-1.78	-9.40

**Table 5.** Comparison between the indentation moduli mean value and amplitude of the modulation calculated with the oscillatory function in Eq. (1) and computed by the Swadener-Pharr method [32] in the axial and transverse direction. Percentage discrepancies are calculated as in Table 4. The orthotropic material model is used.

<b>Indentation Direction</b>	$M_0^{EQ.1}$ [GPa]	$M_0^{COM}$ [GPa]	$\Delta M^{EQ.1}$ [GPa]	$\Delta M^{COM}$ [GPa]	$e_{M0}$ %	$e_{\Delta M}$ %
Axial	26.19	25.80	2.48	2.43	-1.51	-2.02
Transverse	23.56	24.13	5.53	5.77	2.38	4.34

LIST OF SYMBOLS

$A$	axial indentation direction w.r.t. the global coordinate system
$A, T_1, T_2$	global coordinate system (osteons)
$a_1, a_2$	semi-axes lengths of the elliptical projected area of contact
$\mathbf{a}_1, \mathbf{a}_2, \mathbf{a}_3$	indentation coordinate system for the Swadener-Pharr model
$\mathbf{B}$	Barnett-Lothe tensor
$\mathbf{C}$	stiffness tensor
$C_{ijkl}$	stiffness tensor coefficients
$E$	uniaxial Young's modulus
$E_L$	uniaxial Young's modulus along the mineralized collagen fibrils long axis direction
$E_P$	uniaxial Young's modulus perpendicular to the mineralized collagen fibril long axis for a transversely isotropic material model
$E_{P1}, E_{P2}$	uniaxial Young's moduli perpendicular to the mineralized collagen fibril long axis for an orthotropic material model
$G_{LP}$	shear modulus for a mineralized collagen fibril in the L-P plane for a transversely isotropic material model
$G_{LP1}, G_{LP2}, G_{P1P2}$	shear moduli for a mineralized collagen fibril in the L-P <sub>1</sub> , L-P <sub>2</sub> and P <sub>1</sub> -P <sub>2</sub> planes for an orthotropic material model
$L$	longitudinal indentation direction w.r.t. the local coordinate system
$L, P_1, P_2$	local coordinate system (mineralized collagen fibrils)
$M$	indentation modulus
$M_A$	indentation modulus in the axial direction
$M_T$	indentation modulus in the transverse direction
$M_0$	oscillatory function mean value
$M^{exp}$	experimental indentation modulus
$M^{comp}$	indentation modulus computed with the Swadener-Pharr method
$P$	perpendicular indentation direction w.r.t. the local coordinate system
$T$	transverse indentation direction w.r.t. the global coordinate system
$r$	radial position across the osteon
$r_i$	locations corresponding to the peaks and valleys of the stiffness modulation in the axial and transverse directions
$\mathbf{r}, \mathbf{s}, \mathbf{t}$	orthogonal reference system for the Swadener-Pharr model
$w$	lamellar width
$\gamma$	angle between the direction $\mathbf{t}$ and the $\mathbf{a}_1$ axis
$\Delta M$	oscillatory function amplitude
$\theta$	angle between the long axis of the mineralized collagen fibrils and the loading direction
$\nu_{LP}, \nu_{PP}$	Poisson's ratios for a mineralized collagen fibril in the L-P and perpendicular (PP) planes for a transversely isotropic material model
$\nu_{P1L}, \nu_{P2L}, \nu_{P2P1}, \nu_{LP1}, \nu_{LP2}, \nu_{P1P2}$	Poisson's ratios for a mineralized collagen fibril in the L-P <sub>1</sub> , L-P <sub>2</sub> and P <sub>1</sub> -P <sub>2</sub> planes for an orthotropic material model

**SHORT TITLE**

Mechanical Modulation in Cortical Bone

For Review Only

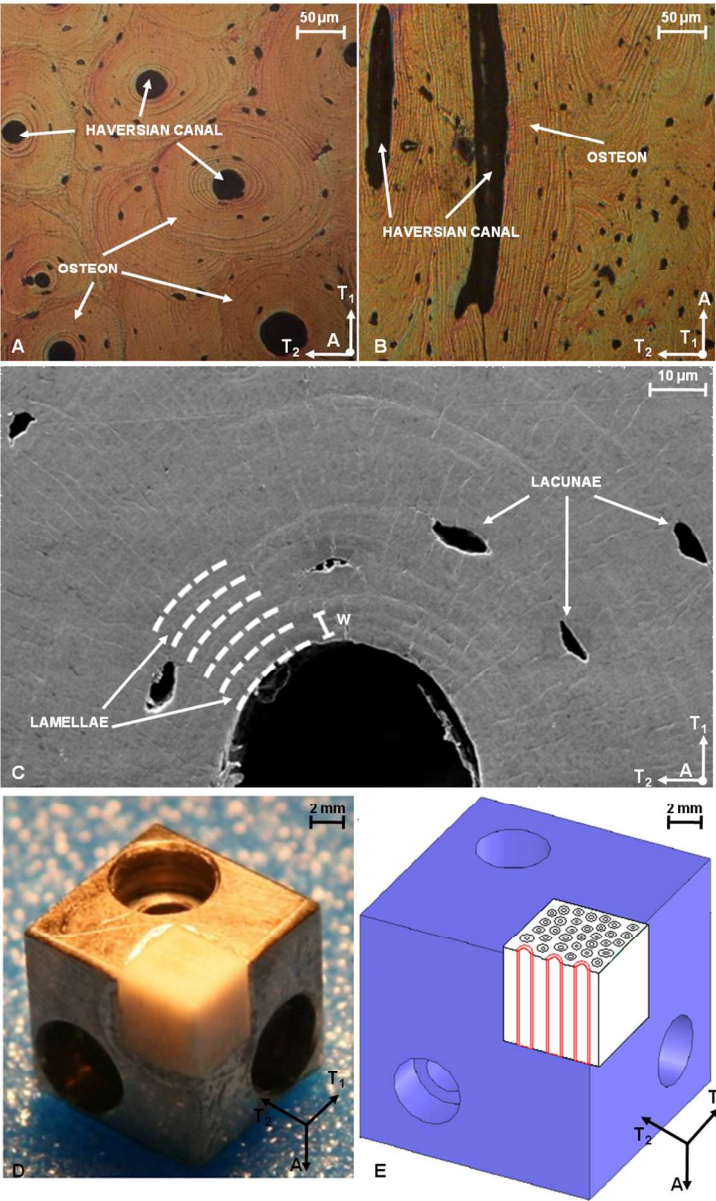


Figure 1  
353x570mm (72 x 72 DPI)

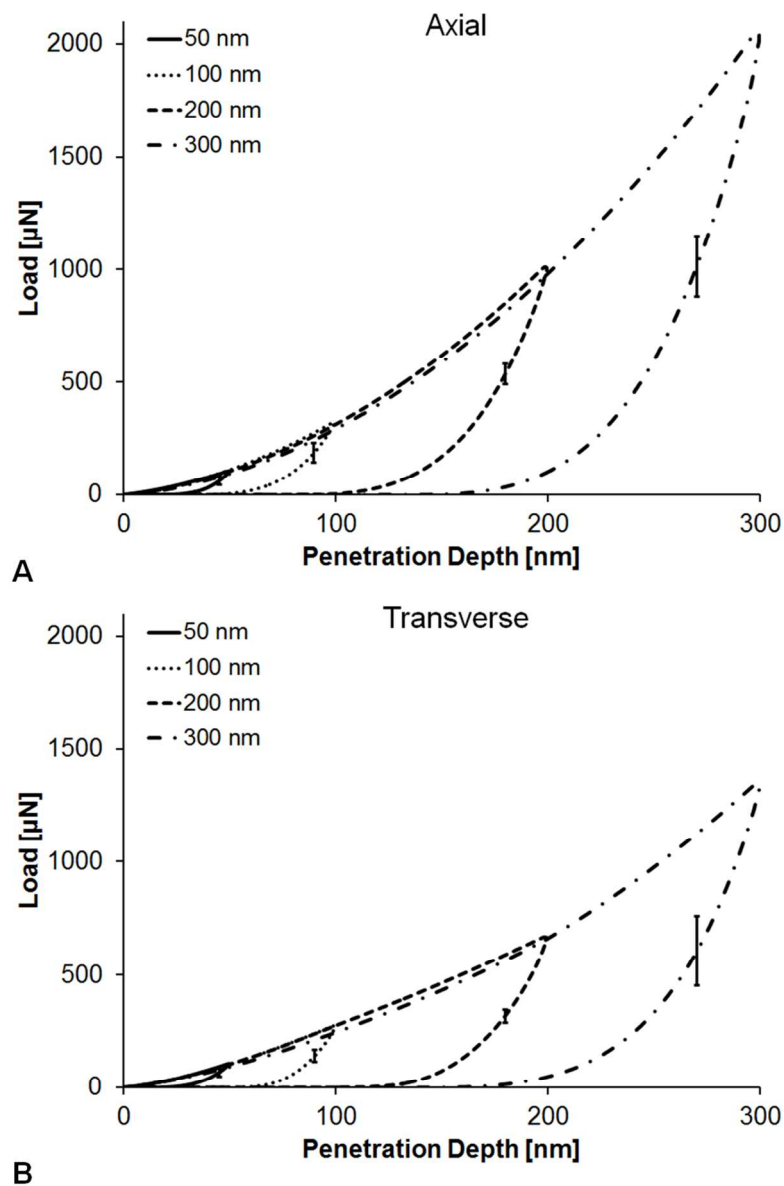


Figure 2  
363x533mm (72 x 72 DPI)

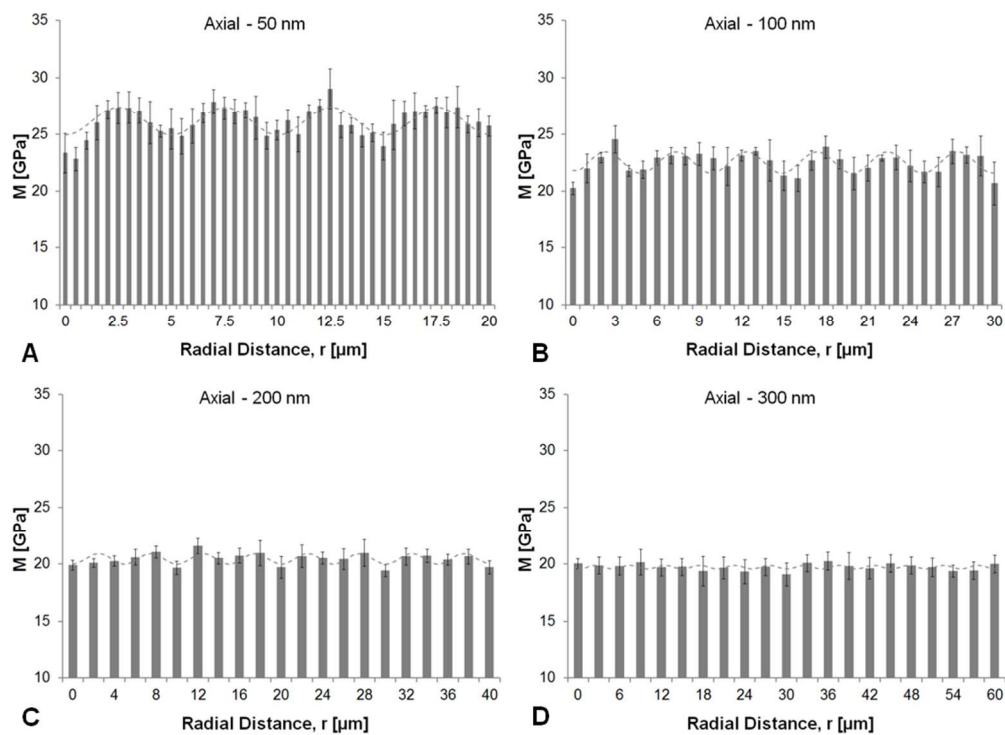


Figure 3  
398x292mm (72 x 72 DPI)

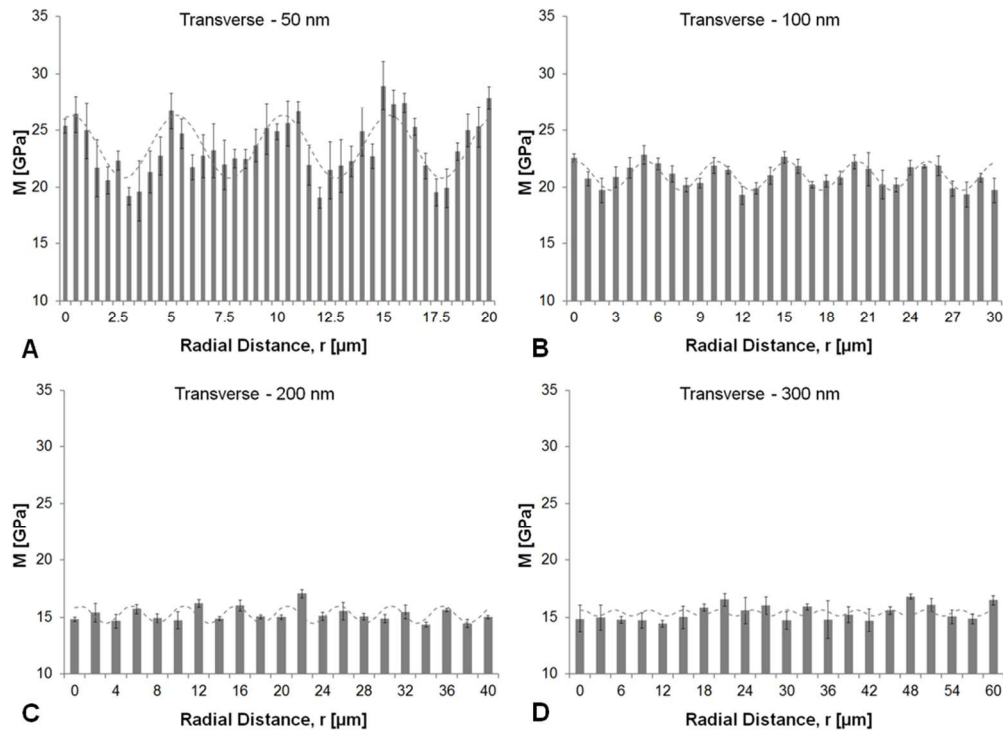


Figure 4  
398x292mm (72 x 72 DPI)

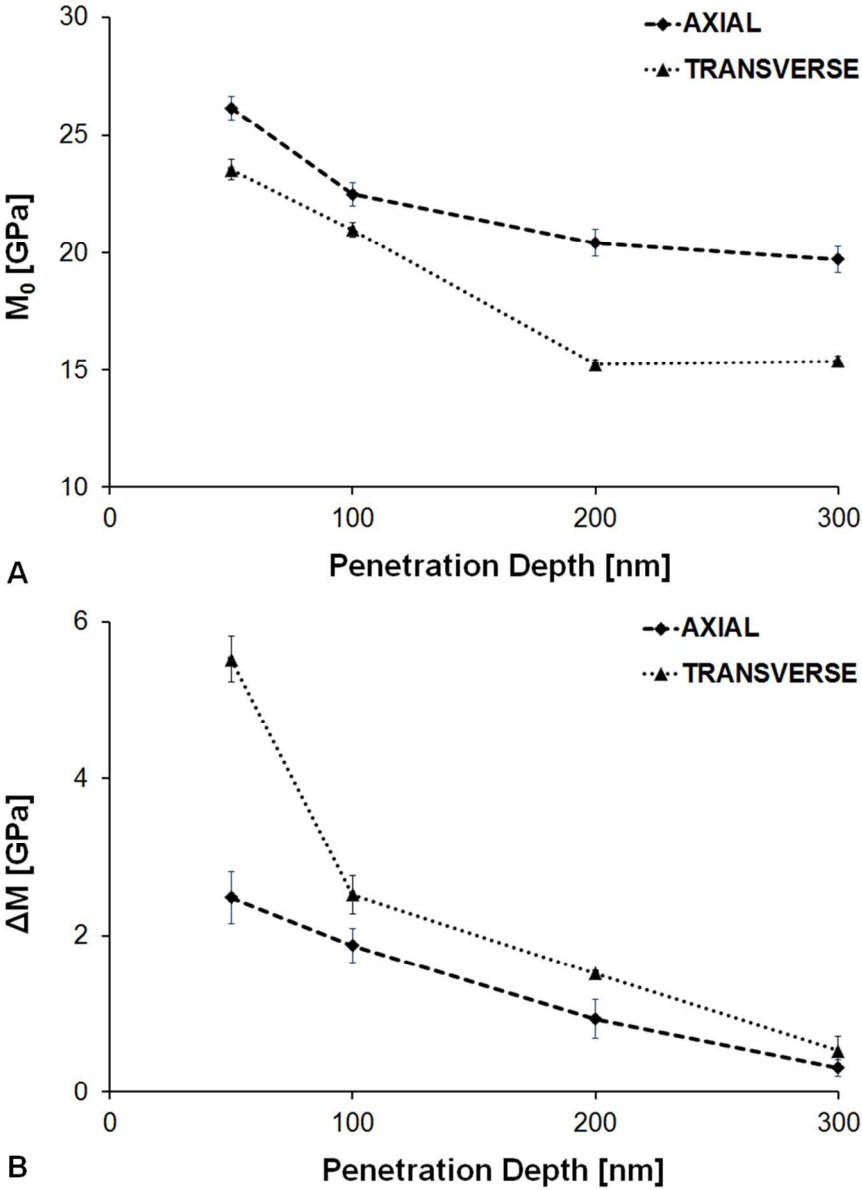


Figure 5  
392x534mm (72 x 72 DPI)

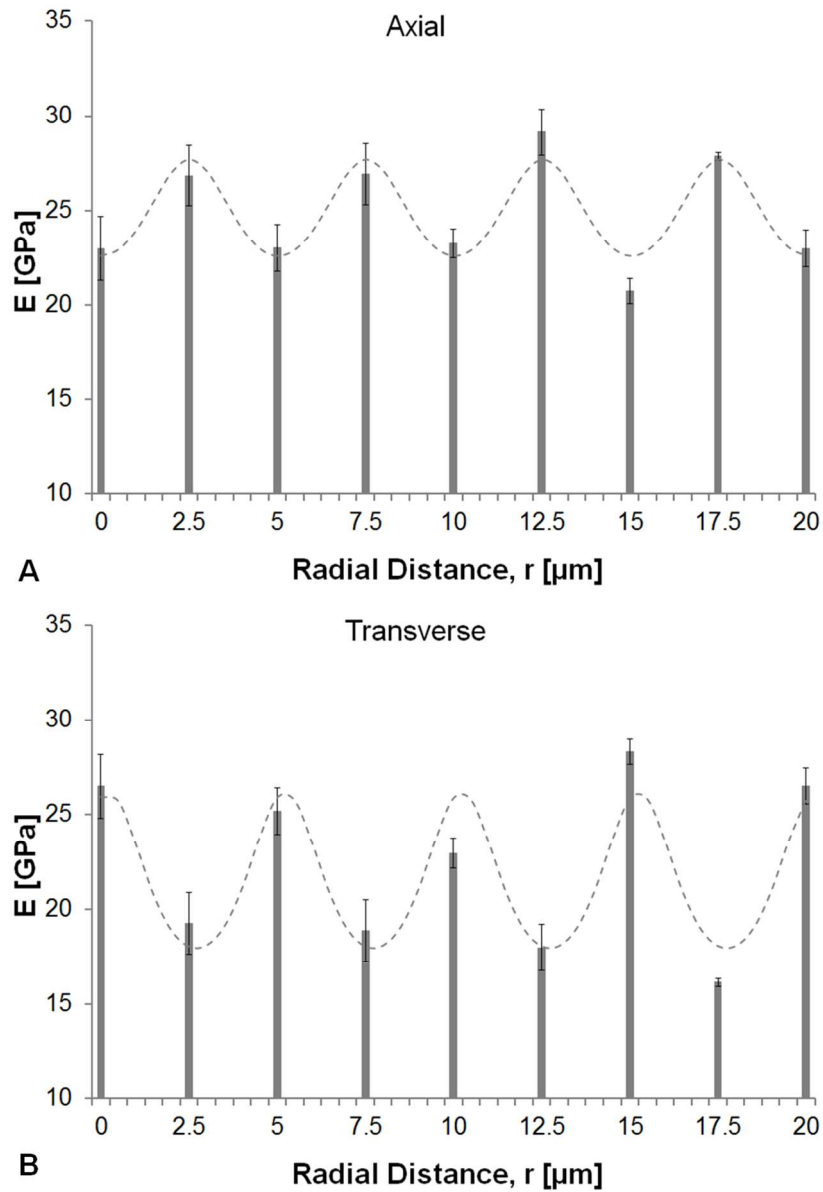


Figure 6  
368x534mm (72 x 72 DPI)

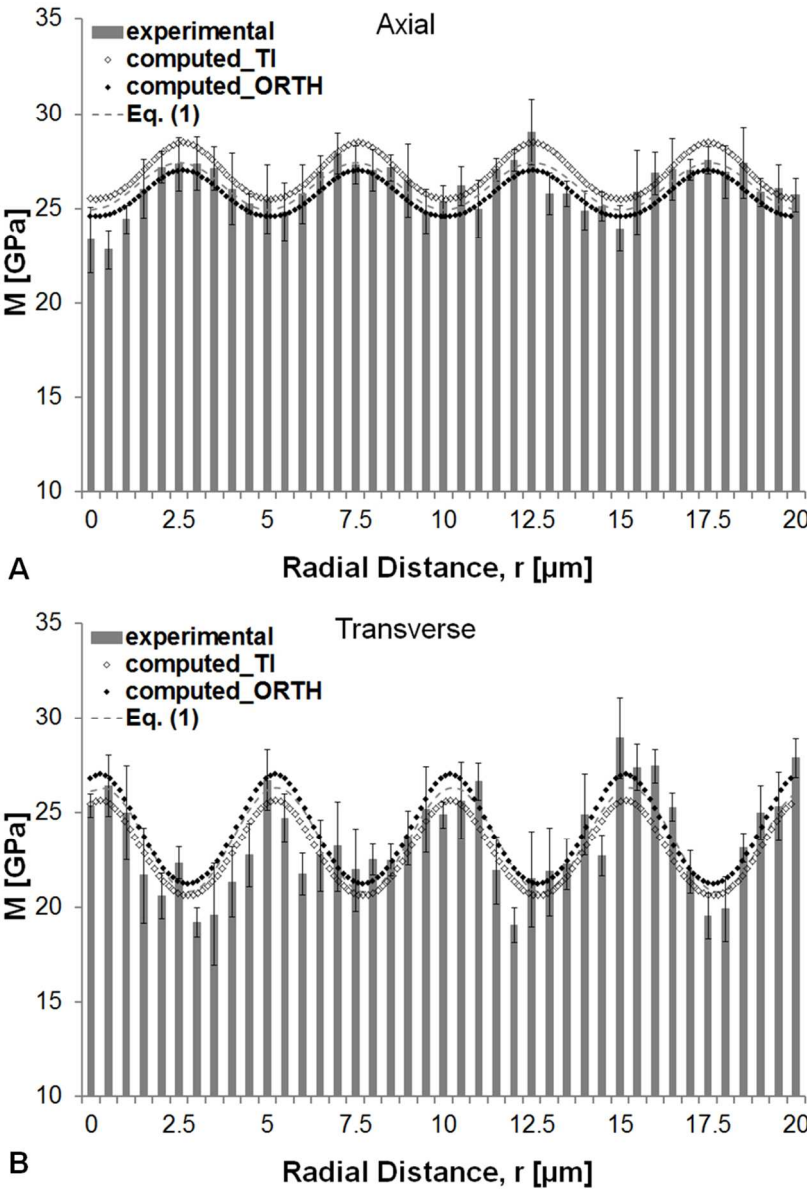


Figure 7  
368x534mm (72 x 72 DPI)

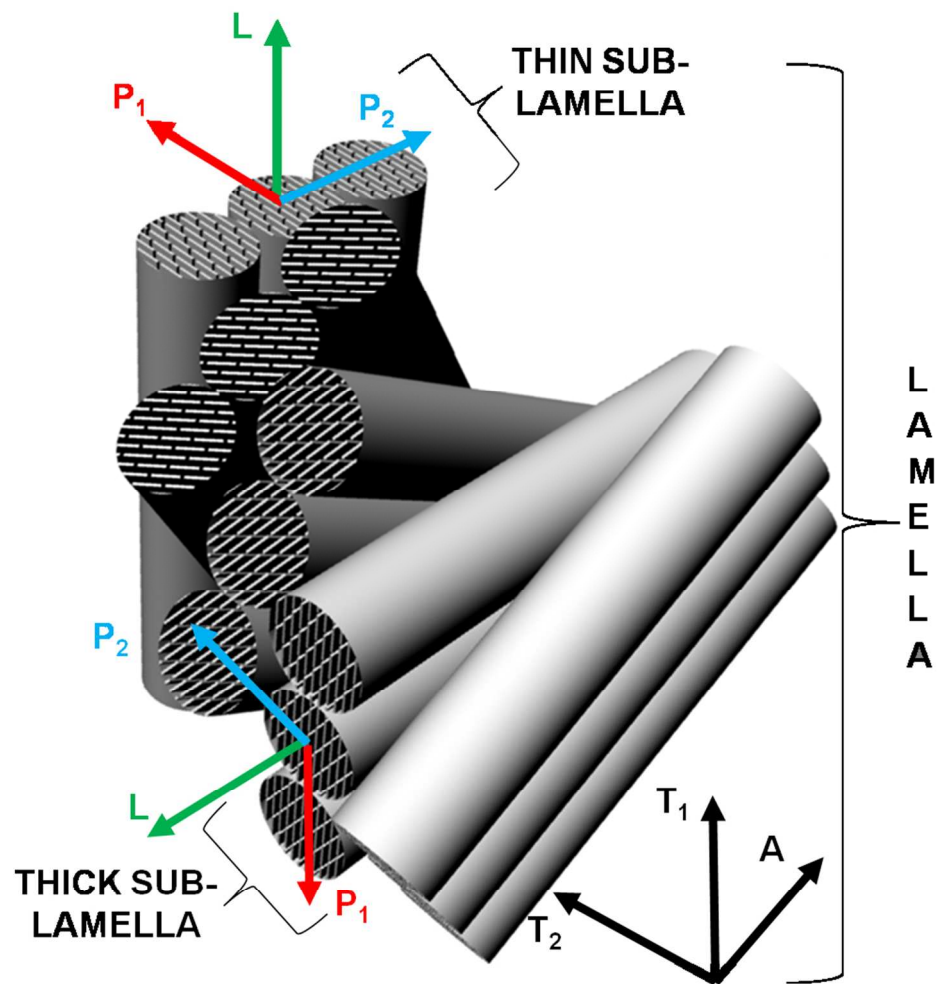


Figure 8  
376x375mm (72 x 72 DPI)

Referee: 1

Comments to the Author

The authors have addressed all the issues raised in my original review. While the paper is of publishable quality at this point, there are a few small details they may choose to address before sending the MS to the publisher.

1. The AFM RMS roughness values seem to be drawn from images that are 30  $\mu\text{m}$  X 30  $\mu\text{m}$  in area. Assuming the standard 512X512 pixel image, this means each pixel is 59 nm X 59 nm. Stating an rms roughness of 6 nm in this case is problematic. For example, if there were oscillations in the surface that were 10 nm in amplitude with a 10 nm period, these would likely sum to an rms of substantially less than 10 nm when integrated over 6 periods. In short, the rms roughness is not dependent only on the z accuracy of the measurement; it is also coupled with the x,y measurements.

We thank the reviewer for the suggestion. We will perform further imaging at higher spatial resolution to confirm the obtained value. In addition, since the penetration depths achieved in the shallowest experiments is 10 times the measured roughness, we expect that uncertainty on the roughness estimation has a little effect on our results.

2. The new text in section 2.1 utilizes one set of units in the body text (mN) and another in the figure caption (fig. 2, ( $\mu\text{N}$ )). This is confusing to the reader.

The values of the mean value and standard deviation of maximum load at 50, 100, 200, and 300 in the axial and transverse directions have been reported in  $\mu\text{N}$  to be consistent with Fig. 2.

3. In section four when the MS refers to 10-20 fibrils fitting in a 2  $\mu\text{m}$  contact patch, the authors are limiting themselves to a one dimensional analysis. If they compute the total area in a 2  $\mu\text{m}$  X 2  $\mu\text{m}$  contact patch and then the total number of fibrils accomodated in this area, I think they will find that there are  $\sim 10\text{X}$  more fibrils being probed.

We agree with the reviewer regarding this observation. The sentence has been modified as: "the largest experimental characteristic length sampled (300 nm maximum depth,  $\sim 2.0 \mu\text{m}$  contact diameter) may accommodate  $\sim 10$  to 20 bunches of collagen fibrils oriented along multiple directions and, thus, involves multiple sub-layers..."

I found it a bit disheartening that, when confronted with arguments supported by publications in well regarded journals, the authors choose not to substantially address the issues of collagen fibril anisotropy and the importance of water in determining the mechanical properties of bone. These are cutting edge issues that have been given substantial attention in the last five years or so. However, if the authors choose to allow these counter arguments to be addressed by others rather than in this manuscript, I can not in good conscience recommend holding up publication of the current work.

We are sorry if the reviewer wasn't completely satisfied in the way we dealt with this particular issue in the present paper and in our answer in the previous response to reviewers. We would just like to underline that some other considerations about hydrated/not hydrated properties of bone tissue can be

found in our previous papers on this topic, and in particular in: Carnelli et al., ASME-Journal of Biomechanical Engineering, 2010, 132, 081008.1-081008.10; Carnelli et al., Journal of Biomechanics, 2011, 44, 1852–1858; and Lucchini et al., Journal of the Mechanical Behaviour of Biomedical Materials, 2011, 4, 1852–1863. We decided not to repeat any of the previously reported considerations in this new paper.

Nevertheless, we agree with the reviewer that the effect of water in determining the mechanical properties of bone is an important issue in the field of bone tissue and we will pay even more attention to this particular topic in the near future.

Note to the Editor:

Please notice that some of the affiliations have been modified in the current version of the manuscript.